Nano-Structures & Nano-Objects 38 (2024) 101156

Contents lists available at ScienceDirect

Nano-Structures & Nano-Objects

journal homepage: www.elsevier.com/locate/nanoso

The antimicrobial and photothermal response of copper sulfide particles with distinct size and morphology

Tina Gulin-Sarfraz [a,*], Laura D'Alfonso [b], Jan-Henrik Smått [c], Giuseppe Chirico [b], Jawad Sarfraz [a,*]

[a] Nofima, Norwegian Institute of Food, Fisheries and Aquaculture Research, P.O. Box 210, NO-1431, Ås, Norway
[b] Department of Physics "G. Occhialini", University of Milano-Bicocca, Piazza della Scienza 3, Milan 20126, Italy
[c] Laboratory of Molecular Science and Engineering, Åbo Akademi University, Henriksgatan 2, Åbo FI-20500, Finland

ARTICLE INFO

Keywords:
Metal chalcogenide
Copper sulfide
Nanostructure
NIR-absorption
Photothermal
Antibacterial activity

ABSTRACT

The development of photothermal agents for antibacterial applications has become increasingly attractive. An exciting area for these materials is in the food industry where such materials can be applied to prevent microbial contamination, as an environment-friendly alternative to chemical disinfectants. However, for such applications, there is a need for low-cost photocatalytic materials with easy synthesis procedures and long-term stability. In this regard, copper sulfide (CuS) nanomaterials have gained vast attention for their large antimicrobial response, driven primarily by the photothermal effect resulting from their uniform absorption in the NIR range. However, an important factor for a successful application is the level of the light-to-heat conversion capability of the specific CuS nanomaterial, which highly impacts on the antimicrobial response. Here, different synthesis procedures were investigated to synthesize a variety of CuS particles with distinct sizes and shapes, to demonstrate the large variation in antimicrobial response. The antibacterial activity of the particles was demonstrated on the bacterium *Escherichia coli* (*E. coli*) by irradiation with a regular IR lamp, to simultaneously investigate light absorption under a relatively low irradiation power. The results reveal that the light absorption of the CuS particles vary greatly and thus also so does the antibacterial effect. In conclusion, the difference in antimicrobial effect can not only be ascribed to size and morphology, but it is also influenced by crystal size and phase composition.

1. Introduction

Recently a great deal of interest has been shown in the photocatalytic properties of carbon-based, metallic and semiconducting materials [1–4]. Among other applications, these materials have the potential to fight antibiotic-resistant bacteria and disinfectant-resistant biofilms [5,6], to be applied for cancer treatment [7–11] and to be utilized for energy production and storage applications [12].

The cases of antibiotic-resistant bacteria are on the rise globally and pose acute danger to the public health. Scientists are constantly looking for new solutions to fight antibiotic-resistant bacteria and the potential of photocatalytic materials is being explored. Several reports confirm that photocatalysts have the potential to be used as antibacterial agents [1–4]. The antimicrobial effect of photocatalytic materials is reported to be governed by their photothermal properties as well as by the production of reactive oxygen species (ROS). Light-triggered antibacterial agents, such as titanium dioxide, graphene-based materials and plasmonic metals, have been frequently reported in the literature [13,14]. However, the need for low-cost photocatalytic materials with easy synthesis procedures, long-term stability and high photoactivity has compelled scientists to look for alternative materials. In this regards, photodynamic and photothermal properties of molybdenum, zinc, copper and other metals oxides have been explored [15–17].

Recently metal sulfides have emerged with interesting photodynamic and photothermal properties. Multiphasic molybdenum disulfide (MoS_2) with photoactivities has been reported for energy production and storage, as well as for light-driven antibacterial applications [18]. MoS_2-based composite materials, for instance MoS_2@Ag and MoS_2@-copper films, have been reported as a water disinfectant under light irradiation against *E. coli* [19,20]. Similarly, a nanocomposite based on MoS_2−ZnO-reduced graphene oxide (GO) has been described to show high antibacterial activity under light irradiation against *S. aureus* and

* Corresponding authors.
E-mail addresses: tina.gulin-sarfraz@nofima.no (T. Gulin-Sarfraz), jawad.sarfraz@nofima.no (J. Sarfraz).

https://doi.org/10.1016/j.nanoso.2024.101156
Received 14 August 2023; Received in revised form 12 March 2024; Accepted 9 April 2024
Available online 13 April 2024

E. coli [21]. Copper sulfide (CuS), which is a narrow bandgap semiconducting material, has also been reported with attractive electrical and optical properties [22]. The absorption of the CuS nanoparticles lies in the NIR region (≈900–1300 nm) originating from the d–d energy band transition of Cu^{2+} ions [23]. CuS has shown effective photothermally induced antimicrobial properties [22]. Composite materials with CuS as one component have also been reported in the literature for antimicrobial applications. For example, a CuS/protonated g-C_3N_4 composite has been shown to exhibit bactericidal effects against both gram-positive and gram-negative bacteria [24]. CuS nanoparticle complex hydrogels have shown complete photothermal bactericidal activity against *S. aureus* and *E coli.* [25].

The potential use of photocatalytic materials in energy production and storage, as well as for biomedical applications, is well documented, as discussed above. An emerging area for these materials is in the food industry where such materials can be utilized to fight disinfectant-resistant biofilms. Chemical disinfectants such as sodium hypochlorite, chlorine dioxide, hydrogen peroxide, peracetic acid, quaternary ammonium compounds, ozone and electrolyzed water are widely used in the food industries to prevent microbial contamination of raw materials and food products [26] to ensure food safety. However, the commercially applied chemical disinfectants have disadvantages, such as their corrosive nature, formation of toxic by-products, unstable and explosive nature, and high cost [26].

The food industry is looking for alternative solutions which are effective, economical and environment-friendly. In this regard, the potential of photocatalytic material-based solutions can be explored. For such applications, low-cost materials with uniform light absorption in the IR range and high capabilities of light-to-heat conversion are of great interest. Here, CuS-based materials are good candidates. However, the level of NIR absorption of these materials is dependent on many factors, such as size, morphology, phase, crystal size and a combination of these. Thus, detailed investigation is needed to understand the large individual variations in the antimicrobial effect of these materials. In this study, we have investigated different synthesis procedures to synthesize a variety of different CuS particles with distinct sizes and shapes to demonstrate the large variation in antimicrobial response. The produced particles were characterized in detail with scanning electron microscopy (SEM), transmission electron microscopy (TEM), X-ray diffraction (XRD), X-ray photoelectron spectroscopy (XPS) and visible-near infrared (Vis-NIR) spectroscopy. Further, the photothermal properties of the particles were evaluated and their antibacterial properties were verified on *E.coli* by irradiation with an IR lamp.

2. Materials and methods

2.1. Materials

Copper(II) nitrate trihydrate ($Cu(NO_3)_2{\cdot}3\ H_2O$), copper(II) chloride dihydrate ($CuCl_2{\cdot}2\ H_2O$), copper(II) acetate hydrate ($Cu(CH_3COO)_2{\cdot}H_2O$), sodium thiosulfate pentahydrate ($Na_2S_2O_3{\cdot}5\ H_2O$), sodium sulfide nonahydrate ($Na_2S{\cdot}9\ H_2O$), sodium citrate monobasic ($NaC_6H_7O_7$), Tween 80 and ethylene glycol (EG) were purchased from Sigma-Aldrich (Merck KGaA, Darmstadt, Germany). Absolute ethanol was obtained from Antibac (Kiilto Oy, Tampere, Finland).

2.2. Synthesis of CuS particles

Different synthesis procedures for CuS particles were investigated to produce particles with distinct sizes and morphologies. The five different synthesized particles were ascribed to flowers (CuS-FL), hexagonal rods (CuS-RD), snowballs (CuS-SB) and nanoparticles (CuS-NP1 and CuS-NP2). The synthesis procedures were derived from the literature [27–29]. The small nanoparticles (CuS-NP1) were selected for their potential efficient heat generation and the flower-shaped particles (CuS-FL) due to their unique structure. The CuS-NP2 particles were chosen as nanoscale reference for the CuS-NP1 particles. Further, the rod-shaped (CuS-RD) and the snowball-shaped (CuS-SB) particles were derived from the CuS-FL and the CuS-NP2 particles, respectively, to adjust the size while keeping a similar morphology without altering the precursors and the synthesis conditions.

Table 1
Synthesis conditions for the different CuS particles. The molar ratio of sodium citrate to Cu was maintained at 0.68:1 for CuS-RD, CuS-SB and CuS-NP1. For CuS-NP2, the pH was adjusted to 6.5 with 1 M HCl.

Sample	Cu-precursor	S-precursor	Solvent, tot V	Temp, time	Na citrate
CuS-FL	2 mmol Cu $(NO_3)_2$	2 mmol $Na_2S_2O_3$	1:3 H_2O-EG 40 mL	70 °C 4 h	No
CuS-RD	2 mmol Cu $(NO_3)_2$	2 mmol $Na_2S_2O_3$	1:3 H_2O-EG 40 mL	70 °C 4 h	Yes
CuS-SB	1 mmol $Cu(CH_3COO)_2$	6 mmol $Na_2S_2O_3$	H_2O, 400 mL	90 °C 6 h	Yes
CuS-NP1	1 mmol $CuCl_2$	1 mmol Na_2S	H_2O 1000 mL	90 °C 15 min	Yes
CuS-NP2	1 mmol Cu $(CH_3COO)_2$	6 mmol $Na_2S_2O_3$	H_2O 400 mL	90 °C 6 h	No

Copper nitrate, copper chloride or copper acetate were used as the copper precursors in combinations with sodium thiosulfate or sodium sulfide, in either water or mixtures of water and ethylene glycol, as presented in Table 1. For CuS-RD, CuS-SB and CuS-NP1, the size and shape were controlled by the addition of sodium citrate (Table 1). The molar ratio of sodium citrate to Cu was kept to 0.68:1 for all synthesis procedures where sodium citrate was added. The synthesis solutions were heated in an oil bath at 70 or 90 °C under constant stirring with reflux. Subsequently, the synthesized particles were cooled down and separated by centrifugation, washed two times with Milli-Q water and vacuum dried.

2.3. Characterization of the CuS particles

2.3.1. Scanning and transmission electron microscopy

Scanning electron microscopy (SEM) and transmission electron microscopy (TEM) were used to study the size and morphology of the different CuS particles. SEM imaging was performed with a Zeiss EVO 50 microscope (Carl Zeiss, Cambridge, UK). Prior to the SEM imaging, dry particles were placed on a carbon tape and further sputter-coated with a gold-palladium alloy with a Polaron SC 7640 sputter coater (Quorum Technologies Ltd, East Sussex, UK). TEM imaging was performed with a JEOL JEM-2100Plus (JEOL Ltd., Tokyo, Japan), with a camera of type TVIPS TemCam-XF416. For TEM imaging, the nanoparticles were dispersed in ethanol at a concentration of 0.1 mg/mL and deposited on holey carbon grids.

2.3.2. X-ray diffraction

The materials were characterized for their crystallinity using X-ray diffraction (XRD). The XRD data was obtained using a Bruker D8 Discover instrument (Bruker AXS GmbH, Karlsruhe, Germany) in the 2θ range 20–60° with a step size of 0.04° and an acquisition time of 3 s/step. The crystallite particle sizes were determined using the Scherrer formula: $D = k\lambda/\beta \cos\theta$. Here, D is the average crystallite size, K is the shape factor (constant, 0.90), λ (1.544 Å) is the wavelength of the CuKα radiation, θ is the Bragg's angle, corresponding to the maximum of the diffraction peak, and β is the full width at half maximum (FWHM) of the diffraction peak measured in radians [29].

2.3.3. X-ray photoelectron spectroscopy

The surface chemical composition of the synthesized materials was analysed with X-ray photoelectron spectroscopy (XPS). XPS spectra were obtained with a Kratos Axis UltraDLD XPS instrument using a

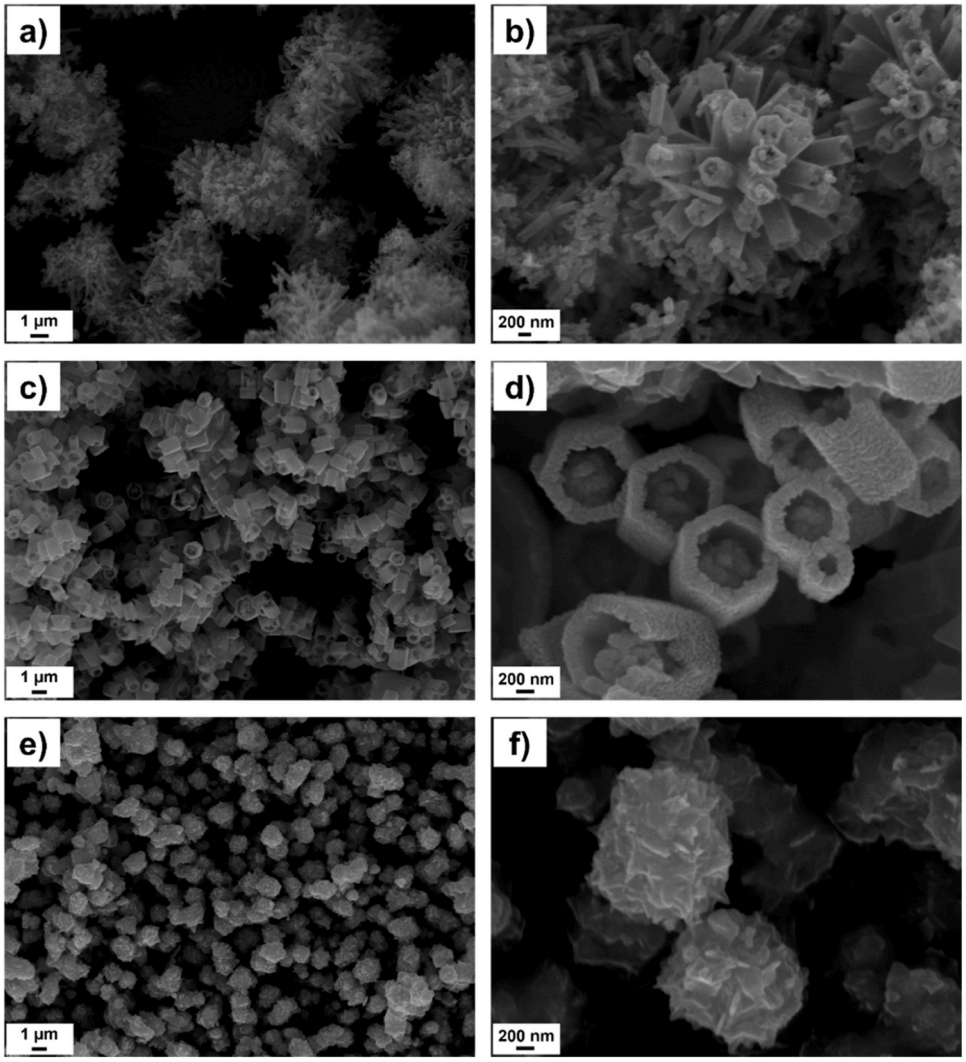

Fig. 1. SEM images of the three different morphologies of the microsized CuS particles. The images present two different magnifications of the particles as follows: a)-b) CuS-FL, c)-d) CuS-RD and e)-f) CuS-SB.

monochromatic Al Kα X-ray source (1486.6 eV) operating at 15 kV and 10 mA at the normal emission angle. For survey and high-resolution spectra, the used pass energy was 80 and 20 eV, respectively. XPS measurements were performed on two separate spots for each sample. The atomic percentage (at%) of the different elements was derived by calculating the area of the peaks and correcting for the sensitivity factors using the CasaXPS software.

2.3.4. Photothermal effect upon near infrared irradiation

The photothermal properties of the drop-cast CuS-particles were characterized using NIR laser irradiation with wavelengths tunable in the 700–980 range (Mai Tai Spectra Physics, Santa Clara, CA, USA). The diameter of the beam spot was set to 12 mm. The temperature changes were monitored by means of a thermo-vision camera (FLIR, E40, Wilsonville, OR, USA) and the supporting analysis software.

The photothermal conversion performance of the samples was evaluated by calculating the specific absorption rate (SAR). Though an exact measure of the photothermal conversion efficiency should be performed under adiabatic conditions [30,31], a lower limit can be provided by computing the SAR coefficient from the faster relaxation component of the thermogram kinetics according to [32]:

$$SAR = \frac{C}{m_{NP}} \left.\frac{dT}{dt}\right|_{t=0} = \frac{C}{m_{NP}} \frac{\Delta T_1}{\tau_1}$$

where C represents the specific heat, m_{NP} the mass, T the temperature, t the time and τ_1 and ΔT_1 represent the relaxation time and temperature amplitude of the faster component of the temperature kinetics. The values were measured at different wavelengths under $I_{exc} \cong 0.2$ W/cm^2 and are reported in kW/kg.

2.3.5. Dynamic light scattering

Dynamic light scattering (DLS) was utilized to evaluate the dispersibility of the CuS particles. The particles were dispersed at a concentration of 0.5 mg/mL by ultrasonication in Milli-Q water or in 0.1 wt % Tween 80, and measured on a Malvern Zetasizer Nano ZS instrument (Malvern Panalytical, Malvern, UK). The measurements were obtained in triplicate and the data are presented as averages.

2.3.6. Visible-near infrared spectroscopy

The absorption properties of the CuS particles dispersed in 0.1 wt% Tween 80 at a concentration of 0.5 mg/mL were studied by utilizing visible-near infrared (Vis-NIR) spectroscopy. The absorption spectra were obtained using a FOSS NIRSystems XDS Rapid Content™ Analyzer (FOSS Analytical A/S, Hillerød, Denmark). The spectral range measured was from 400 to 2500 nm with 0.5 nm increments. However, for a comparison of the absorption properties of the different CuS particles, the spectral range from 400 to 1400 nm was used since it covers the

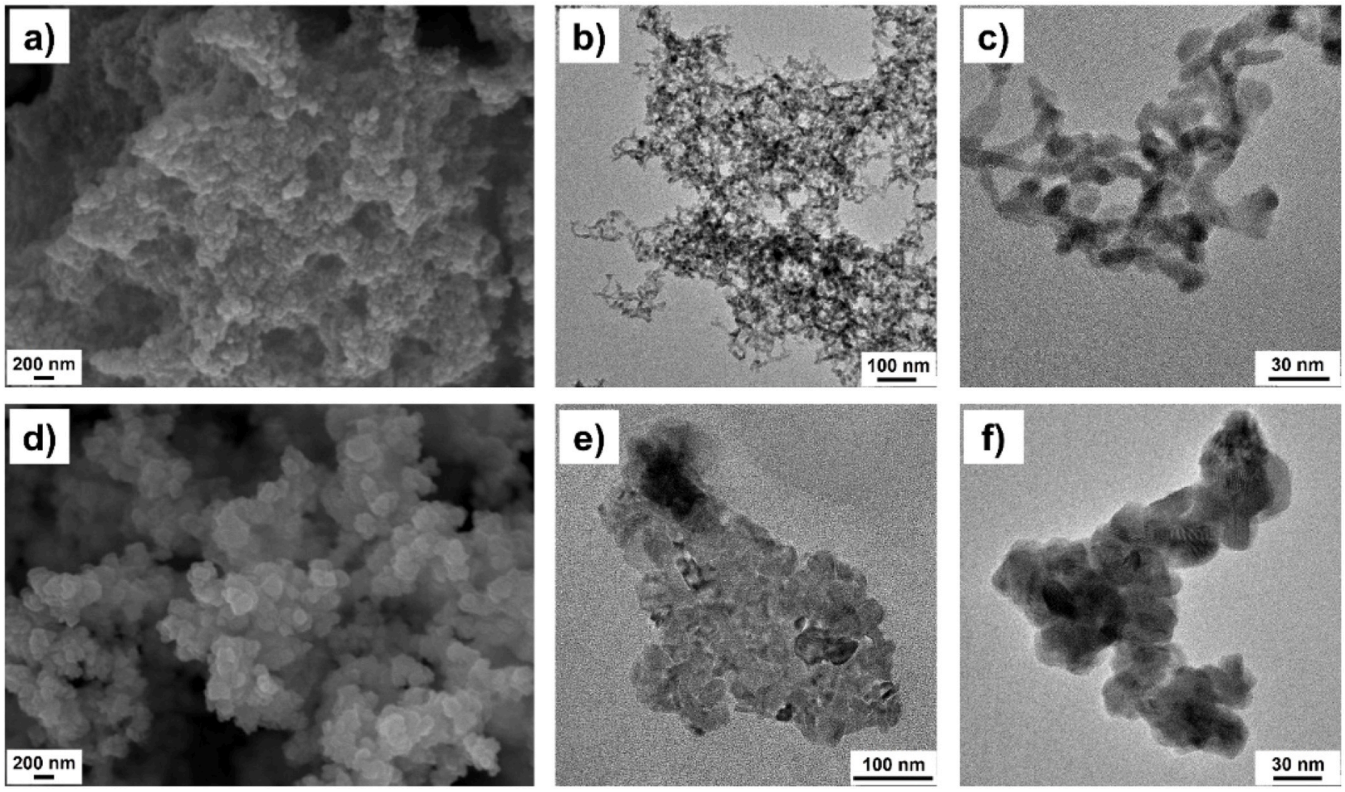

Fig. 2. SEM and TEM images of the two different CuS nanoparticles, where the upper row (a-c) presents CuS-NP1 and the lower row (d-f) CuS-NP2.

relevant absorption range for CuS.

2.3.7. Antimicrobial response

The antibacterial properties of the CuS particles were examined under a conventional 150 W IR lamp, which covers the whole IR spectra but has the highest relative spectral power in the range of 700–1300 nm. The lamp was placed at a 35 cm distance from the samples and the antimicrobial response was evaluated against *Escherichia coli* (BL21DE3 strain), since this strain has previously been used for similar studies [22,33]. The bacteria were grown in tryptone soya broth, TSB, (Oxoid, Basingstoke, UK) overnight at 37 °C and 150 rpm. A suspension containing approximately 1×10^8 colony-forming units (CFU)/mL was prepared in TSB containing 0.1 wt% Tween 80. The CuS particles were dispersed in TSB (containing 0.1 wt% Tween 80 to aid the dispersion of the particles) by ultrasonication. On 12-well plates 1.8 mL particle dispersions were mixed with 0.2 mL bacteria suspension, to have a final concentration of 0.3 mg/mL particles and 1×10^7 CFU/mL. Prior to the NIR irradiation, the plates were incubated at 37 °C, 80 rpm, for one hour. After this, the plates to be irradiated were taken out and placed under the IR lamp for 8 min under continuous shaking at 80 rpm. Further, the plates were incubated for another 15 min at 37 °C, 80 rpm, to reach normal temperature. The bacteria suspensions were diluted and plated on tryptone soya agar plates by the Whitley Automated Spiral Plater, WASP (Don Whitley Scientific Ltd., Shipley, UK). The viable bacteria number after incubation at 37 °C for 24 h was determined by counting the CFUs. All the experiments were performed in duplicate.

3. Results and discussion

3.1. Characterization of the size and morphology of the CuS particles

CuS particles with different morphologies in the micro- and nano-size range were produced by utilizing various precursors and synthesis conditions. Scanning electron microscopy (SEM) images of the microsized particles are shown in Fig. 1. The distinct and controlled morphology of these samples have been ascribed to flowers (CuS-FL) (Fig. 1a and b), hexagonal rods (CuS-RD) (Fig. 1c and d) and snowballs (CuS-SB) (Fig. 1e and f). Transmission electron microscopy (TEM) and SEM images of the nanosized particles are presented in Fig. 2, showing their very small size in the range of 10–30 nm in diameter. The electron microscopy images further reveal a slightly different shape of CuS-NP2 (Fig. 2d-f). These are not spherical, but have rather sharp edges. The same sharp edges are seen on CuS-SB, which are derived from a similar synthesis procedure as CuS-NP2.

3.2. X-ray diffraction studies

X-ray diffraction (XRD) was employed to determine the crystalline phase compostion and crystallite size of the CuS particles. The diffraction patterns of the different samples are presented in Fig. 3. Fig. 3a shows the diffraction patterns of the CuS-NP2 and CuS-SB samples, which can be grouped together as they display similar patterns. The main diffraction peaks can be indexed to a pure hexagonal covellite phase of CuS, with lattice constants a = 3.79 Å and c = 16.34 Å [34]. While CuS-SB does not show any other phases, sample CuS-NP2 contains some trace amounts of hydrated copper sulfates, namely bonattite ($Cu(SO_4)_2 \bullet 3\ H_2O$) as well as chalcanthite ($Cu(SO_4)_2 \bullet 5\ H_2O$).

Similarly, Fig. 3b shows the diffractograms of the CuS-FL and CuS-NP1 samples, which display similar patterns in terms of peak positions. Both samples consist of covellite CuS as the main phase with substantial amounts of the bonattite ($Cu(SO_4)_2 \bullet 3\ H_2O$) phase. Finally, Fig. 3c shows that the CuS-RD sample consists mainly of the CuS covellite phase with fair amounts of the chalcanthite ($Cu(SO_4)_2 \bullet 5\ H_2O$) phase.

Theoretically, it should be possible to estimate the crystallite size from the XRD peak broadening. From the (102) reflection at ~29.3°, the covellite crystallite size of samples CuS-SB and CuS-NP2 can be estimated as 31.3 and 18.5 nm, respectively. However, due to overlapping

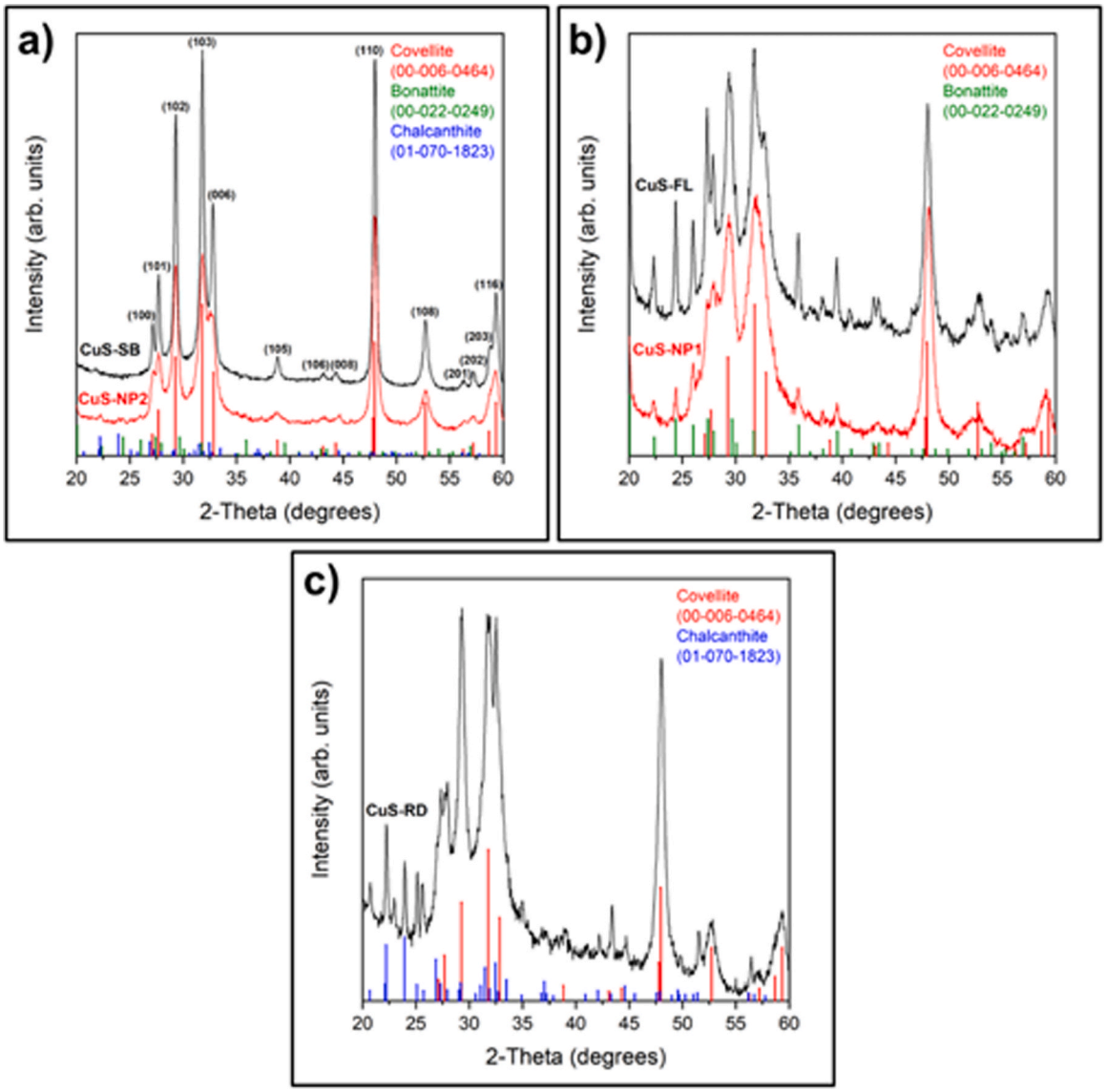

Fig. 3. XRD data of the different CuS samples investigated in this study: a) CuS-SB and CuS-NP2, b) CuS-FL and CuS-NP1, and c) CuS-RD. Reference patterns of covellite, bonattite and chalcanthite are included for comparison.

peaks from the hydrated copper sulfates phase, it is not possible to accurately determine the covellite crystallite size for the other samples. Nonetheless, the covellite crystallite size seems to decrease in the following order: CuS-SB > CuS-NP2 > CuS-RD > CuS-FL > CuS-NP1, based on the peak broadening.

3.3. X-ray photoelectron spectroscopy

X-ray photoelectron spectroscopy (XPS) is a highly surface-sensitive analytical technique used to study the elemental composition, chemical state and electronic state of materials to a depth of about 10 nm [35]. Here, both survey spectra and high-resolution spectra were measured at two different spots for all the different particles synthesized. The atomic concentrations of the detected elements for each sample are presented in Supplementary Table ST1. The ratio between sulfur and copper is 3.5 ±0.5 for all the microsized particles. For the nanoparticles, the ratio is slightly lower, around 2.1 for CuS-NP1 and approximately 2.8 for CuS-NP2. Fig. 4a shows the survey spectra of the different particles with the identified carbon, oxygen, copper and sulfur peaks. Impurities such as chlorine, nitrogen and sodium were not detected.

The atomic percentage of copper lies in the range of 9±3 at% for all the samples, except for CuS-NP1 where the concentration of copper was considerably higher at 23.5±1.5 at% (Supplementary Table ST1). For CuS-NP1, sodium sulfide is used as a sulfur precursor instead of sodium thiosulfate. This seems to influence the surface properties of the resulting particles. The CuS-NP1 particles were less prone to the adsorption of atmospheric impurities, as confirmed by the amount of detected carbon, discussed below. The high concentration of copper for CuS-NP1 can be further explained by their relatively small size. Fig. 4b shows the high-resolution spectra of copper. Copper peaks $Cu2p^{3/2}$ at a binding energy of 932.5±0.3 eV and $Cu2p^{1/2}$ at 952.2±0.3 eV confirm that the detected copper is bound with sulfur in the form of copper sulfide [36,37]. There are no differences observed in the shape and position of the $Cu2p^{3/2}$ and $Cu2p^{1/2}$ peaks. Interestingly, shake-up satellite peaks representative of Cu^{2+} at around 945 eV were not observed, suggesting that copper is in the form of Cu^{+} [38,39]. It has been reported in the literature that the copper in covellite CuS is in the form of Cu^{+} rather than Cu^{2+}, while S has various valencies, such as S^{2-} and S_2^{-} [40,41].

Like copper, a significantly higher amount of sulfur (50±2 at%) is detected for CuS-NP1 compared to the other particles. Fig. 4c shows the high-resolution spectra of sulfur. The sulfur peak at 162.4±0.4 eV is

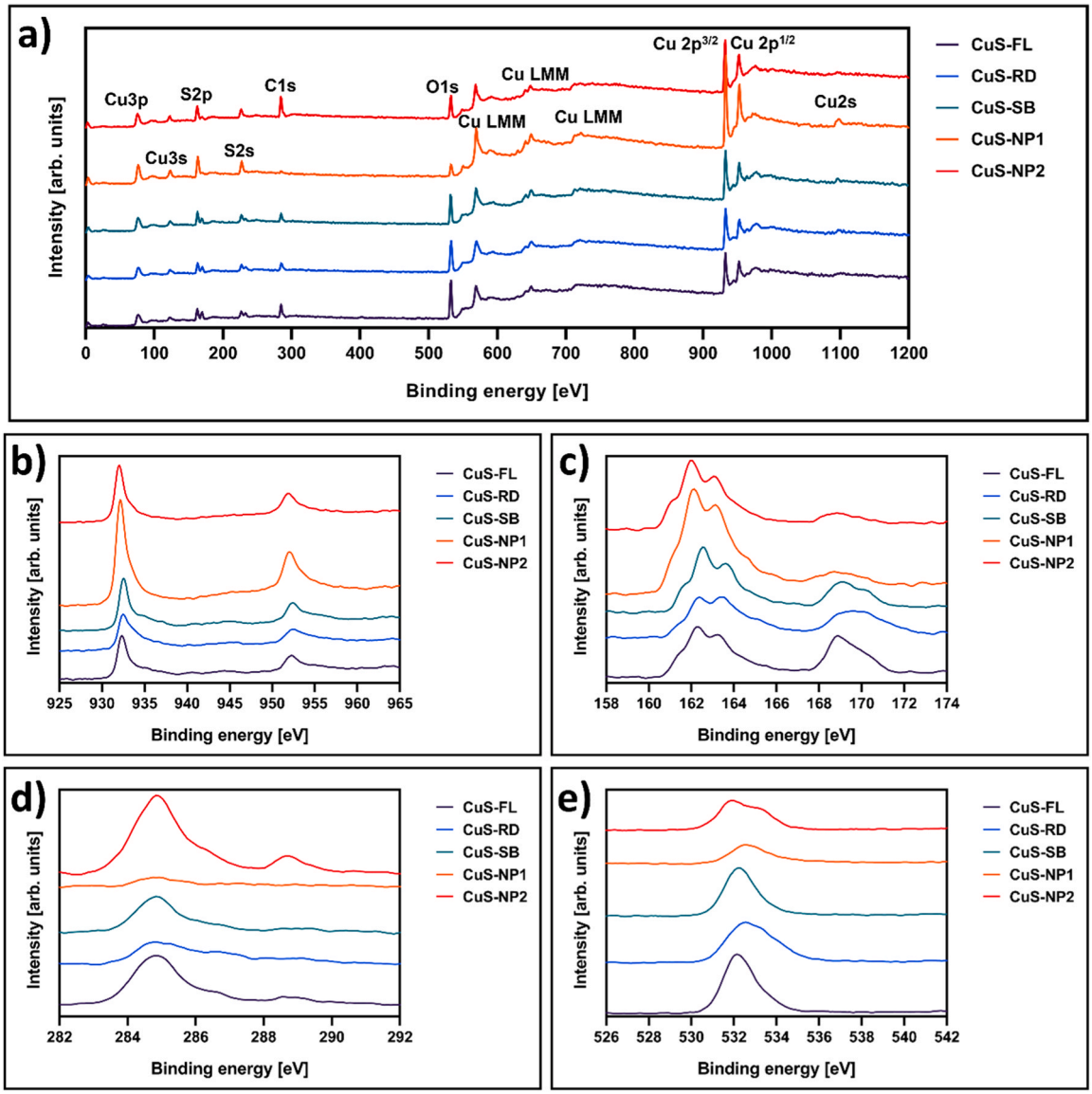

Fig. 4. (a) XPS survey spectra of CuS-FL, CuS-RD, CuS-SB, CuS-NP1 and CuS-NP2, with identified peaks from carbon, copper, sulfur and oxygen. High-resolution spectra of copper (b), sulfur (c), carbon (d) and oxygen (e).

rather broad, possibly resulting from the overlapping of different peaks. The observed sulfur peak can be associated to mono-sulfides and di-sulfide bonded with Cu^{+1} and Cu^{+2} centers [42]. The peak at 169 ±0.4 eV can be associated with $CuSO_4$ [42]. Significant differences are observed in the intensities of the sulfur peaks for different samples; however, the peak positions were not affected. The sulfate peak is detected for all samples; however, it is more prominent for CuS-FL, CuS-RD and CuS-SB. The higher amount of sulfate can be explained by surface oxidation, which probably also explains the higher amount of detected oxygen for the microsized particles. Here it is important to mention that we did not observe sulfate in the XRD pattern for CuS-SB. Since XRD is a bulk method, surface oxidation products are more difficult to detect with XRD compared to XPS.

Carbon was detected for all the samples. However, the amount of detected carbon seems to be affected by the used sulfur precursor and sodium citrate. CuS-NP1 showed the least amount of surface carbon. These are the only particles where sodium sulfide was used as a sulfur precursor instead of sodium thiosulfate. Furthermore, it can be seen in Table 1 and Supplementary Table ST1 that the use of sodium citrate suppresses the amount of surface carbon. The origin of carbon can be either from remaining solvent, from copper acetate or most likely impurities adsorbed from the atmosphere [43]. It is plausible that the surface area and morphology also affect the adsorption of atmospheric carbon. Fig. 4d shows the high-resolution spectra of carbon, where the C1s peak is evident. The main peak at binding energies close to 285 ±0.3 eV is rather broad for all the samples indicating that in addition to C-C, it might be that carbon is also present in the form of C-C-OH. It is interesting to observe from Fig. 4d that only CuS-NP2 has a clear peak at a higher binding energy of 289 eV. Even though clear differences were observed in the high-resolution carbon peaks for CuS-NP1 and CuS-NP2, no significant differences are observed in the copper and sulfur peaks for these two particles, except for the peak intensities. The C1s peaks are attributable to atmospheric oxidation and absorption of atmospheric moisture [22]. As further shown in Supplementary Table ST1, the atomic concentration of oxygen was much higher for the microsized samples (in the range of 32±3 at%) compared to CuS-NP1 (17.4 at%) and CuS-NP2 (20±1 at%). Fig. 4e shows the high-resolution spectra of oxygen, where the O1s peak at a binding energy of 532.2±0.3 eV is visible.

To summarize, the elemental compositions of the microsized

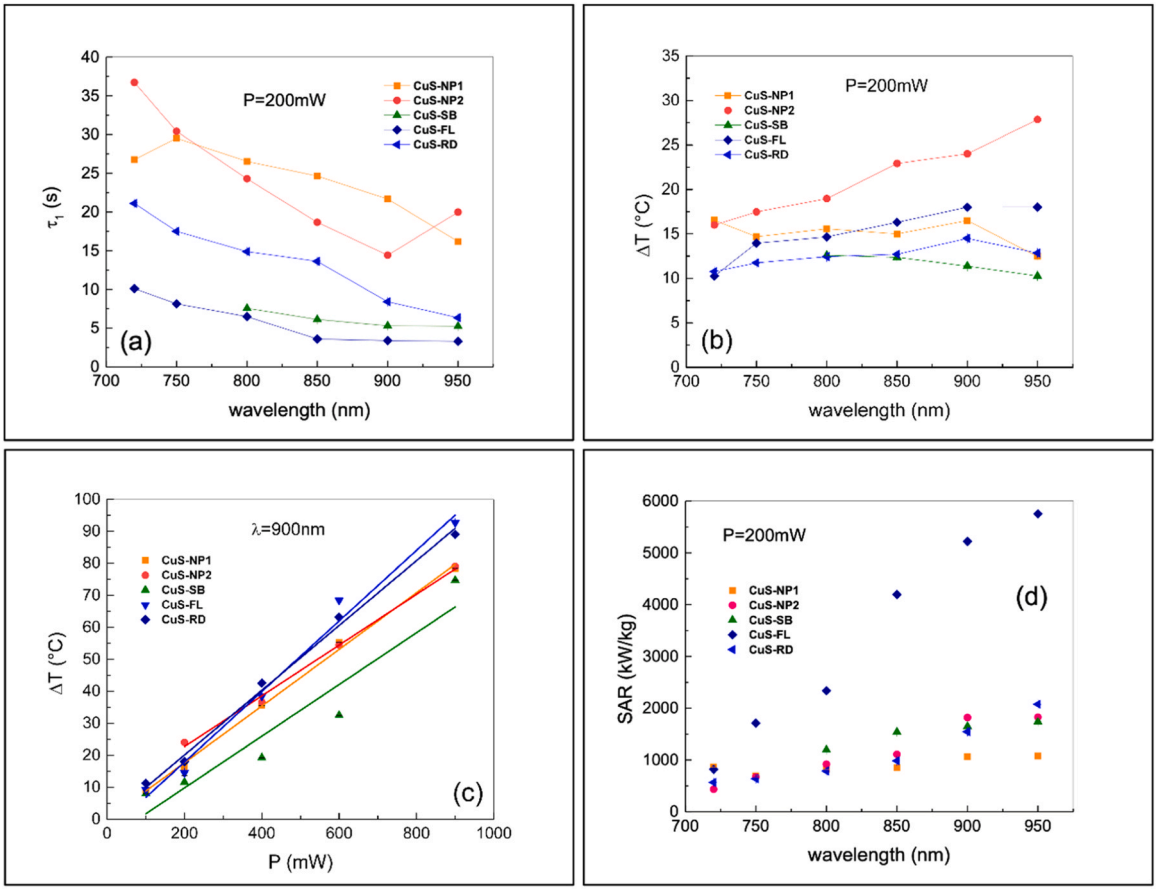

Fig. 5. Photothermal characterization of the samples. The rise time and temperature increase as a function of the irradiation wavelength (at power = 200 mW) are presented in (a) and (b). The change in temperature as a function of the irradiation power at λ = 900 nm is shown in (c), and the specific absorption rate (SAR) as a function of the irradiation wavelength is presented in (d).

particles were rather similar. A significantly higher amount of carbon was detected for CuS-NP2 and considerably higher amounts of copper and sulfur were detected for CuS-NP1, compared to the other particles. Interestingly, despite the differences in the at% of copper and sulfur between the two nanoparticles (CuS-NP1 and CuS-NP2), the ratio between copper and sulfur was rather similar.

3.4. Photothermal properties

The photothermal performances of the CuS particles were investigated by NIR laser irradiation. For all the samples, the temperature increased rapidly, followed by a plateau, and the temperature increase as a function of the irradiation time was fitted to double exponential growth curves, as exemplified with the CuS-NP2 sample in Supplementary Figure SF1. The laser wavelengths were varied in the range from 720 to 950 nm, and the power was adjusted from 100 to 900 mW.

The heating kinetics of the different particles under NIR irradiation is described by the short time characteristic of the specific sample (τ_1), as presented in Fig. 5a. The samples were irradiated at different wavelengths with a low laser power of only 200 mW, corresponding to a laser intensity of about 0.17 W/cm^2. At shorter wavelengths the fast rise time varied widely between the different samples, from 10 to 37 seconds, while at longer wavelengths the rise time was less than 20 seconds for all the samples. However, the shortest rise time was observed for the CuS-FL sample, where the plateau was already reached within 3–4 seconds at higher wavelengths (850–950 nm). Further, a decrease of the heating characteristic time was observed for all the samples when irradiating with longer wavelengths, except for the CuS-NP2 particles, which again increased at higher wavelengths (900–950 nm). At wavelengths lower than 800 nm, with a power of 200 mW, no significant and reproducible increase of the local temperature was detected for the CuS-SB sample.

The temperature increase (ΔT) as a function of wavelength was fairly constant for CuS-RD and CuS-SB, as shown in Fig. 5b. However, for CuS-FL and the two nanoparticle samples (CuS-NP1 and CuS-NP2), the total temperature increase was higher and it also varied with the different wavelengths. For samples CuS-FL and CuS-NP2, the decrease of the heating characteristic time up to 900 nm (Fig. 5a) anticorrelated nicely with the increase of the photothermal effect (Fig. 5b). When the irradiation power was varied at a wavelength of 900 nm, the measured temperature increase was linear for all samples, showing no saturation effects in the power range investigated, even though CuS-SB gave rise to a large jump in temperature at high power (900 mW), as shown in Fig. 5c.

Moreover, the photothermal conversion efficacy of the different samples was assessed by comparing their specific absorption rates (SAR), as presented in Fig. 5d. The SAR describes the particles capability in absorbing energy per unit mass. A high value of the SAR is desired for a large generation of heating load in the sample. As seen in Fig. 5d, CuS-FL gives rise to larger SAR values at longer wavelengths, with values of 6000 kW/kg at 950 nm, compared to the other particles that display fairly similar values in the range of 1000 kW/kg $\leq SAR \leq$ 2000 kW/kg at 950 nm. The SAR values for all the samples are listed in Supplementary Table ST2.

3.5. Dispersibility of the particles and their optical properties

To utilize the CuS particles as dispersions, for instance to study their antimicrobial properties, the dispersions need to be stable for a sufficient

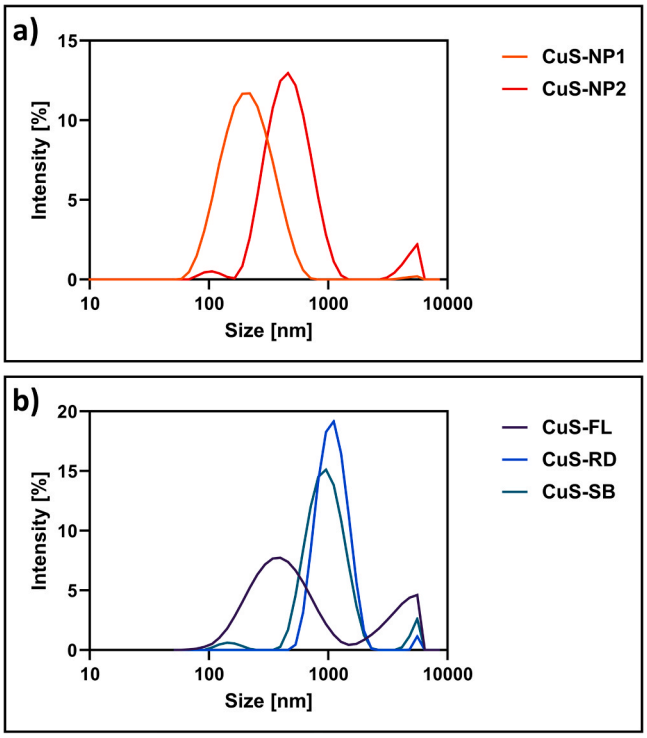

Fig. 6. Hydrodynamic size distributions of (a) the nanoparticles and (b) the microsized particles.

time. Since pure CuS particles aggregate in water, a widely used surface active agent, Tween 80, was utilized for the dispersions. Considering the antimicrobial experiments, the concentration of Tween 80 was kept to a minimum so as not to affect the growth of the bacteria. Thus, a concentration of 0.1 wt% water-solution of Tween 80 was found to stabilize several types of the particles. The dispersibility of the particles were measured by dynamic light scattering, by comparing the particles dispersed in water and in the Tween 80 solution. The results are presented in Supplementary Figures SF2-SF5, where a large shift of the size distributions towards smaller sizes can be seen when the dispersibility of the particles is facilitated by Tween 80. This is especially pronounced for the nanoparticle samples. The size distributions of the nanoparticles CuS-NP1 and CuS-NP2 are further presented in Fig. 6a, which reveal the dispersibility of these particles by their narrow size distributions, where only some minor aggregates are shown for the sample CuS-NP2. However, their hydrodynamic size is clearly larger than their actual size observed by electron microscopy. This is a well-known challenge with the DLS technique when analysing particles like CuS, which give rise to large absorbance and scattering of the light, subsequently giving rise to errors in the size calculations [44–47]. Even so, DLS is a useful tool for studying the dispersibility and stability of the particles. Further, the dispersed nanoparticles were followed over time and were observed to be stable in the dispersion for a sufficient period of time, as shown in Supplementary Figure SF2.

The dispersibility of the microsized particles, as presented in Fig. 6b, reveal clearly larger size distributions of the CuS-RD and the CuS-SB samples. These two samples showed a tendency to form larger aggregates which were not influenced significantly by the low concentration of the dispersing agent. A fast aggregation and sedimentation of these samples were observed, as presented in Supplementary Figures SF4 and SF5. However, CuS-FL was dispersed to a higher degree, even though with a wide size distribution and an additional peak at larger sizes (Fig. 6b). The larger size distribution of this sample was also indicated from the SEM images (Fig. 1a and b). The dispersion of the CuS-FL particles was stable for a sufficient time, as shown in Supplementary Figure SF3. After 30 min, only some larger aggregates had sedimented.

The optical properties of the CuS dispersions were validated by Vis-NIR spectroscopy (Fig. 7). CuS-FL and both of the nanoparticles (CuS-NP1 and CuS-NP2) show high absorption in the NIR region. CuS-FL and the CuS-NP1 have a maximum at around 1000 nm, while CuS-NP2 has the highest absorbance at around 1200 nm. The redshift from 1000 to 1200 nm can be explained by the larger crystal size of CuS-NP2 compared to CuS-FL and CuS-NP1, as previously reported for CuS nanocrystals of various sizes [48]. In addition, these three samples give rise to a high absorption peak at 400 nm. In accordance with the photothermal measurements performed on drop-cast particles by lasers, which revealed a constant ΔT for CuS-RD and CuS-SB through the whole measured region, the absorbance values for these two samples also do not change here with the wavelength.

3.6. *Antibacterial properties*

Photothermal materials with high capabilities of light-to-heat conversion have become increasingly attractive, since these can reduce the amount of laser energy required [49]. Previous studies have reported that the level of absorption is highly dependent on the size [22], morphology [50] and thus the specific surface area [51] of the CuS nanostructures. In this study, the photothermally-induced antimicrobial effect of the different CuS-particles was investigated on *E.coli* by irradiation with a regular IR lamp, to simultaneously explore the light absorption of the particles under a relatively low irradiation power.

To evaluate the antimicrobial performance, the bacteria were individually mixed with the particles in liquid media, incubated with or

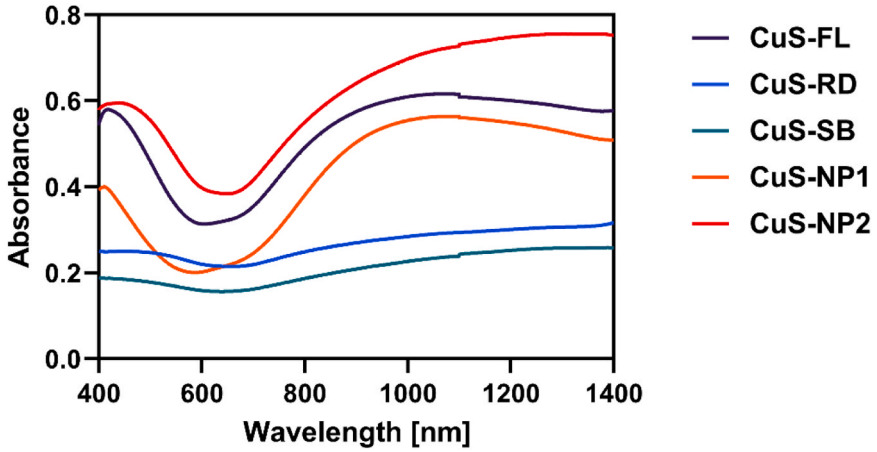

Fig. 7. Absorbance of the CuS dispersions (0.5 mg/mL) in the visible (400–700 nm) and NIR (700–1400 nm) wavelength ranges.

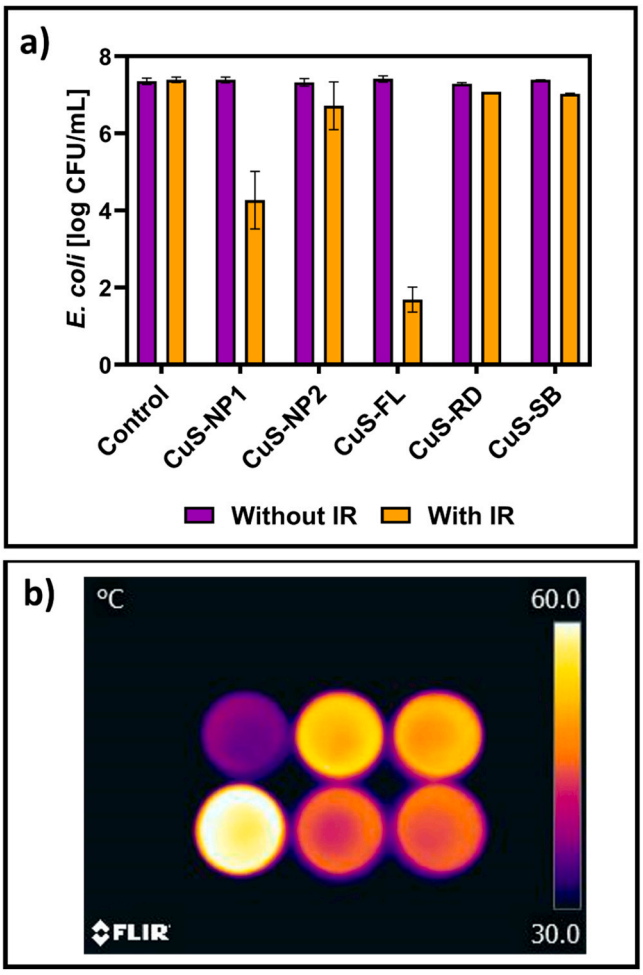

Fig. 8. (a) Antimicrobial response of the different CuS particles on *E.coli*, with and without IR irradiation (8 min). The particles do not show any antibacterial activity in the absence of IR irradiation. (b) Thermal images of the samples in the following order from left to right; Control, CuS-NP1, CuS-NP2 (upper row), CuS-FL, CuS-RD, CuS-SB (lower row).

without IR irradiation for 8 min and subsequently spread on agar plates to analyse the growth of the bacteria. The total viable counts of the bacteria are presented in Fig. 8a, while Fig. 8b shows the corresponding temperature increase of the samples. Previously, it has been reported that for efficiently defeating bacteria or cancer cells, hyperthermic temperatures of around 45 °C are required [2,52]. More specifically, *E. coli* have been shown to lose their viability at temperatures $\geq$ 50 °C [1]. Here, the average temperatures of the samples after 8 min of IR exposure were as follows: control (media without particles) 37 °C, CuS-NP1 53 °C, CuS-NP2 51 °C, CuS-FL 59 °C, CuS-RD 45 °C and CuS-SB 46 °C (Fig. 8b). The antimicrobial response of the different particles follows the same trend as the temperature increase. The microsized CuS-FL sample exhibited the highest antimicrobial response (Fig. 8a), together with the largest temperature increase (Fig. 8b). This sample was followed by the relatively large antimicrobial effect of CuS-NP1, a much smaller effect of CuS-NP2 and almost no antimicrobial effect of the two microsized samples, CuS-RD and CuS-SB. This trend seems to be closely related to the covellite crystallite size of the samples, which decreased in the following order: CuS-SB > CuS-NP2 > CuS-RD > CuS-FL > CuS-NP1, as determined by XRD. Thus, a small crystallite size seems to be beneficial for a photothermally-induced antimicrobial response, independent of the size of the whole particle, probably due to a large accessible surface area. The importance of the size of the nanocrystals has also been demonstrated in other studies, showing a size-dependent photothermal effect of CuS nanodots [53], gold nanoparticles [54] and silicon quantum dots [55].

Further, it is known that CuS nanomaterials produce reactive oxygen species (ROS) when irradiated with simulated solar light [22]. However, it has also been demonstrated that CuS nanoparticles produce ROS when excited by NIR light only [56,57]. Two possible mechanisms of ROS production due to NIR irradiation have been described [56]; the first one is that heat alone generates ROS, since heat can activate dissolved oxygen, and the second is that the copper ions released from the CuS nanomaterial accelerate ROS production by working as a redox active agent. The release of copper ions in a biological system is a pH dependent process. However, in a previous study it was demonstrated that the formation of $CuSO_4$ on the surfaces of CuS nanoparticles, by oxidation of sulfide ions to sulfate, can change the properties of the nanoparticles by increasing solubility and copper ion dissolution [40]. This might have influenced the antimicrobial effect of CuS-FL and CuS-NP1 since both of these particles have a large amount of bonattite, as revealed by XRD. Further, when the CuS nanomaterials are partially oxidized, the absorption intensity is enhanced as well as the absorption peak being narrowed [55]. As a conclusion, even though CuS nanomaterials are reported to have a stable absorption in the NIR region, where the level of absorption is dependent on the size and morphology, their NIR-induced antimicrobial effect may also be greatly influenced by other properties, such as crystallite size and oxidation products.

4. Conclusion

In the present study, five different CuS particles with various physicochemical properties were produced, by utilizing various precursors and synthesis conditions. The particles were characterized in detail with the aim to demonstrate the large variation in the light-induced antimicrobial activity. Previously it has been demonstrated that smaller nanoparticles are more efficient in generating heat than their larger counterparts, with a subsequent higher antimicrobial activity. Even though the CuS-FL particles were of the micronsize (the largest sized particles in this study), they reached the highest temperature, of almost 60 °C, by irradiation with a conventional IR lamp. This followed well with the calculated SAR value, which was considerable higher for CuS-FL than for the other particles, at longer wavelengths. The high temperature increase of CuS-FL was followed by a >5-log reduction in growth of the *E.coli*. However, the temperature increase of the smallest nanoparticles studied, CuS-NP1, were also remarkable and gave rise to a 3-log reduction of the bacteria. The CuS-NP2, CuS-RD and CuS-SB particles gave none or a very small inhibitory effect. The antimicrobial response of the different particles appeared to be closely related to the covellite crystallite size of the samples, which decreased in the following order: CuS-SB > CuS-NP2 > CuS-RD > CuS-FL > CuS-NP1. In addition, the CuS-FL and CuS-NP1 particles contained a noticeable amount of bonattite, which previously has been demonstrated to potentially increase the copper ion dissolution. An increase in the number of copper ions may accelerate ROS production and thus positively influence the antimicrobial response.

As a conclusion, the NIR-induced antimicrobial effect of CuS nanomaterials has gained vast attention and is primarily driven by the photothermal effect resulting from the uniform NIR-absorption of CuS. However, the antimicrobial effect is not only related to the size and/or morphology of the CuS particles, but is also associated with the inner crystallite size, the resulting accessible surface area as well as the oxidation products. Thus, a detailed investigation of the material is needed to design the most suitable material for a specific application.

CRediT authorship contribution statement

Tina Gulin-Sarfraz: Conceptualization, Investigation, Methodology, Validation, Visualization, Writing – original draft, Writing – review & editing. **Laura D'Alfonso**: Investigation, Validation, Visualization,

Writing – review & editing. **Jan-Henrik Smått**: Investigation, Resources, Validation, Visualization, Writing – review & editing. **Giuseppe Chirico**: Resources, Validation, Writing – review & editing. **Jawad Sarfraz**: Conceptualization, Investigation, Methodology, Project administration, Validation, Visualization, Writing – original draft, Writing – review & editing, Resources, Supervision, Funding acquisition.

Declaration of Competing Interest

The authors declare that they have no known competing financial interests or personal relationships that could have appeared to influence the work reported in this paper.

Data Availability

Data will be made available on request.

Acknowledgements

The authors would like to thank Anette Wold Åsli for her skilful technical assistance on the antimicrobial experiments. Hilde Raanaas Kolstad at the Imaging Centre, Norwegian University of Life Sciences (NMBU) is greatly acknowledged for the proficient TEM imaging and the technical assistance on the SEM imaging. The graphical abstract was created with BioRender.com. The study was funded by the Research Council of Norway through the project NanoFunPack grant no 302243, and Norwegian Fund for Research Fees for Agricultural Products (FFL) through the project FutureFoodControl grant no 314743.

Appendix A. Supporting information

Supplementary data associated with this article can be found in the online version at doi:10.1016/j.nanoso.2024.101156.

References

[1] S. Yougbaré, H.-L. Chou, C.-H. Yang, D.I. Krisnawati, A. Jazidie, M. Nuh, T.-R. Kuo, Facet-dependent gold nanocrystals for effective photothermal killing of bacteria, J. Hazard. Mater. 407 (2021) 124617.
[2] S. Yougbaré, C. Mutalik, D.I. Krisnawati, H. Kristanto, A. Jazidie, M. Nuh, T.-M. Cheng, T.-R. Kuo, Nanomaterials for the photothermal killing of bacteria, Nanomaterials 10 (6) (2020) 1123.
[3] T.-K. Chang, T.-M. Cheng, H.-L. Chu, S.-H. Tan, J.-C. Kuo, P.-H. Hsu, C.-Y. Su, H.-M. Chen, C.-M. Lee, T.-R. Kuo, Metabolic mechanism investigation of antibacterial active cysteine-conjugated gold nanoclusters in Escherichia coli, ACS Sustain. Chem. Eng. 7 (18) (2019) 15479–15486.
[4] H. Chen, B. Wang, D. Gao, M. Guan, L. Zheng, H. Ouyang, Z. Chai, Y. Zhao, W. Feng, Broad-spectrum antibacterial activity of carbon nanotubes to human gut bacteria, Small 9 (16) (2013) 2735–2746.
[5] M. Borzenkov, P. Pallavicini, A. Taglietti, L. D'Alfonso, M. Collini, G. Chirico, Photothermally active nanoparticles as a promising tool for eliminating bacteria and biofilms, Beilstein J. Nanotechnol. 11 (1) () (2020) 1134–1146.
[6] P. Grisoli, L. De Vita, C. Milanese, A. Taglietti, Y. Diaz Fernandez, M. Bouzin, L. D'Alfonso, L. Sironi, S. Rossi, B. Vigani, PVA films with mixed silver nanoparticles and gold nanostars for intrinsic and photothermal antibacterial action, Nanomaterials 11 (6) (2021) 1387.
[7] Q. Tian, F. Jiang, R. Zou, Q. Liu, Z. Chen, M. Zhu, S. Yang, J. Wang, J. Wang, J. Hu, Hydrophilic Cu9S5 nanocrystals: a photothermal agent with a 25.7% heat conversion efficiency for photothermal ablation of cancer cells in vivo, ACS Nano 5 (12) (2011) 9761–9771.
[8] Z. Yang, Z. Sun, Y. Ren, X. Chen, W. Zhang, X. Zhu, Z. Mao, J. Shen, S. Nie, Advances in nanomaterials for use in photothermal and photodynamic therapeutics, Mol. Med. Rep. 20 (1) (2019) 5–15.
[9] K. Kannan, D. Radhika, K.K. Sadasivuni, K.R. Reddy, A.V. Raghu, Nanostructured metal oxides and its hybrids for photocatalytic and biomedical applications, Adv. Colloid Interface Sci. 281 (2020) 102178.
[10] Z. Liu, Q. Xu, Y. Li, W. Chen, Fluorescent C-dot nanocomposites as efficient photothermal agents and multi-modal imaging tracers, Mater. Chem. Front. 1 (3) (2017) 538–541.
[11] G. Song, M. Kenney, Y.-S. Chen, X. Zheng, Y. Deng, Z. Chen, S.X. Wang, S. S. Gambhir, H. Dai, J. Rao, Carbon-coated FeCo nanoparticles as sensitive magnetic-particle-imaging tracers with photothermal and magnetothermal properties, Nat. Biomed. Eng. 4 (3) (2020) 325–334.
[12] X. Chen, C. Li, M. Grätzel, R. Kostecki, S.S. Mao, Nanomaterials for renewable energy production and storage, Chem. Soc. Rev. 41 (23) (2012) 7909–7937.
[13] T.-R. Kuo, H.-J. Liao, Y.-T. Chen, C.-Y. Wei, C.-C. Chang, Y.-C. Chen, Y.-H. Chang, J.-C. Lin, Y.-C. Lee, C.-Y. Wen, Extended visible to near-infrared harvesting of earth-abundant FeS2–TiO2 heterostructures for highly active photocatalytic hydrogen evolution, Green. Chem. 20 (7) (2018) 1640–1647.
[14] M.S. Irshad, N. Arshad, X. Wang, Nanoenabled photothermal materials for clean water production, Glob. Chall. 5 (1) (2021) 2000055.
[15] Q. Wei, Y. Wang, H. Qin, J. Wu, Y. Lu, H. Chi, F. Yang, B. Zhou, H. Yu, J. Liu, Construction of rGO wrapping octahedral Ag-Cu2O heterostructure for enhanced visible light photocatalytic activity, Appl. Catal. B: Environ. 227 (2018) 132–144.
[16] C. Mutalik, Y.-C. Hsiao, Y.-H. Chang, D.I. Krisnawati, M. Alimansur, A. Jazidie, M. Nuh, C.-C. Chang, D.-Y. Wang, T.-R. Kuo, High uv–vis–nir light-induced antibacterial activity by heterostructured TiO2-FeS2 nanocomposites, Int. J. Nanomed. (2020) 8911–8920.
[17] C. Mutalik, D.-Y. Wang, D.I. Krisnawati, A. Jazidie, S. Yougbare, T.-R. Kuo, Light-activated heterostructured nanomaterials for antibacterial applications, Nanomaterials 10 (4) (2020) 643.
[18] C. Mutalik, D.I. Krisnawati, S.B. Patil, M. Khafid, D.S. Atmojo, P. Santoso, S.-C. Lu, D.-Y. Wang, T.-R. Kuo, Phase-dependent MoS2 nanoflowers for light-driven antibacterial application, ACS Sustain. Chem. Eng. 9 (23) (2021) 7904–7912.
[19] C. Liu, D. Kong, P.-C. Hsu, H. Yuan, H.-W. Lee, Y. Liu, H. Wang, S. Wang, K. Yan, D. Lin, Rapid water disinfection using vertically aligned MoS2 nanofilms and visible light, Nat. Nanotechnol. 11 (12) (2016) 1098–1104.
[20] P. Cheng, Q. Zhou, X. Hu, S. Su, X. Wang, M. Jin, L. Shui, X. Gao, Y. Guan, R. Nożel, Transparent glass with the growth of pyramid-type MoS2 for highly efficient water disinfection under visible-light irradiation, ACS Appl. Mater. Interfaces 10 (28) (2018) 23444–23450.
[21] A. Priyadharsan, S. Shanavas, V. Vasanthakumar, B. Balamuralikrishnan, P. Anbarasan, Synthesis and investigation on synergetic effect of rGO-ZnO decorated MoS2 microflowers with enhanced photocatalytic and antibacterial activity, Colloids Surf. A: Physicochem. Eng. Asp. 559 (2018) 43–53.
[22] C. Mutalik, G. Okoro, D.I. Krisnawati, A. Jazidie, E.Q. Rahmawati, D. Rahayu, W.-T. Hsu, T.-R. Kuo, Copper sulfide with morphology-dependent photodynamic and photothermal antibacterial activities, J. Colloid Interface Sci. 607 (2022) 1825–1835.
[23] J. Sarfraz, M. Borzenkov, E. Niemelä, C. Weinberger, B. Törngren, E. Rosqvist, M. Collini, P. Pallavicini, J. Eriksson, J. Peltonen, Photo-thermal and cytotoxic properties of inkjet-printed copper sulfide films on biocompatible latex coated substrates, Appl. Surf. Sci. 435 (2018) 1087–1095.
[24] H. Ding, D. Han, Y. Han, Y. Liang, X. Liu, Z. Li, S. Zhu, S. Wu, Visible light responsive CuS/protonated g-C3N4 heterostructure for rapid sterilization, J. Hazard. Mater. 393 (2020) 122423.
[25] L. Zhou, F. Chen, Z. Hou, Y. Chen, X. Luo, Injectable self-healing CuS nanoparticle complex hydrogels with antibacterial, anti-cancer, and wound healing properties, Chem. Eng. J. 409 (2021) 128224.
[26] L. Yuan, F.A. Sadiq, N. Wang, Z. Yang, G. He, Recent advances in understanding the control of disinfectant-resistant biofilms by hurdle technology in the food industry, Crit. Rev. Food Sci. Nutr. 61 (22) (2021) 3876–3891.
[27] J. Kundu, D. Pradhan, Controlled synthesis and catalytic activity of copper sulfide nanostructured assemblies with different morphologies, ACS Appl. Mater. Interfaces 6 (3) (2014) 1823–1834.
[28] M. Zhou, R. Zhang, M. Huang, W. Lu, S. Song, M.P. Melancon, M. Tian, D. Liang, C. Li, A chelator-free multifunctional [64Cu] CuS nanoparticle platform for simultaneous micro-PET/CT imaging and photothermal ablation therapy, J. Am. Chem. Soc. 132 (43) (2010) 15351–15358.
[29] S. Yadav, P. Bajpai, Synthesis of copper sulfide nanoparticles: pH dependent phase stabilization, Nano-Struct. Nano-Obj. 10 (2017) 151–158.
[30] H. Mamiya, B. Jeyadevan, Hyperthermic effects of dissipative structures of magnetic nanoparticles in large alternating magnetic fields, Sci. Rep. 1 (1) (2011) 157.
[31] S. Huang, S.Y. Wang, A. Gupta, D.A. Borca-Tasciuc, S.J. Salon, On the measurement technique for specific absorption rate of nanoparticles in an alternating electromagnetic field, Meas. Sci. Technol. 23 (3) (2012) 035701.
[32] S. Freddi, L. Sironi, R. D'Antuono, D. Morone, A. Donà, E. Cabrini, L. D'Alfonso, M. Collini, P. Pallavicini, G. Baldi, D. Maggioni, G. Chirico, A molecular thermometer for nanoparticles for optical hyperthermia, Nano Lett. 13 (5) (2013) 2004–2010.
[33] C. Mutalik, G. Okoro, H.-L. Chou, I.-H. Lin, S. Yougbaré, C.-C. Chang, T.-R. Kuo, Phase-dependent 1T/2H-MoS2 nanosheets for effective photothermal killing of bacteria, ACS Sustain. Chem. Eng. 10 (27) (2022) 8949–8957.
[34] W. Feng, W. Nie, Y. Cheng, X. Zhou, L. Chen, K. Qiu, Z. Chen, M. Zhu, C. He, In vitro and in vivo toxicity studies of copper sulfide nanoplates for potential photothermal applications, Nanomed. Nanotechnol. Biol. Med. 11 (4) (2015) 901–912.
[35] M.C. Krueger, B. Seiwert, A. Prager, S. Zhang, B. Abel, H. Harms, D. Schlosser, Degradation of polystyrene and selected analogues by biological Fenton chemistry approaches: Opportunities and limitations, Chemosphere 173 (2017) 520–528.
[36] B.R. Strohmeier, D.E. Levden, R.S. Field, D.M. Hercules, Surface spectroscopic characterization of CuAl2O3 catalysts, J. Catal. 94 (2) (1985) 514–530.
[37] J. Sarfraz, A. Fogde, P. Ihalainen, J. Peltonen, The performance of inkjet-printed copper acetate based hydrogen sulfide gas sensor on a flexible plastic substrate-varying ink composition and print density, Appl. Surf. Sci. 445 (2018) 89–96.
[38] V. Hayez, A. Franquet, A. Hubin, H. Terryn, XPS study of the atmospheric corrosion of copper alloys of archaeological interest, Surface and Interface Analysis: An International Journal devoted to the development and application of techniques for the analysis of surfaces, Interfaces Thin Films 36 (8) (2004) 876–879.

[39] V.B. Llorente, V.M. Dzhagan, N. Gaponik, R.A. Iglesias, D.R. Zahn, V. Lesnyak, Electrochemical tuning of localized surface plasmon resonance in copper chalcogenide nanocrystals, J. Phys. Chem. C. 121 (33) (2017) 18244–18253.
[40] S.W. Goh, A.N. Buckley, R.N. Lamb, Copper (II) sulfide? Miner. Eng. 19 (2) (2006) 204–208.
[41] H. Wu, V.W. Or, S. Gonzalez-Calzada, V.H. Grassian, CuS nanoparticles in humid environments: adsorbed water enhances the transformation of CuS to CuSO4, Nanoscale 12 (37) (2020) 19350–19358.
[42] E. Kurmaev, V. Fedorenko, V. Galakhov, S. Bartkowski, S. Uhlenbrock, M. Neumann, P. Slater, C. Greaves, Y. Miyazaki, Analysis of oxyanion (BO33−, CO32−, SO42−, PO43−, SeO44-) substitution in Y123 compounds studied by X-ray photoelectron spectroscopy, J. Supercond. 9 (1996) 97–100.
[43] B. Pejjai, M. Reddivari, T.R.R. Kotte, Phase controllable synthesis of CuS nanoparticles by chemical co-precipitation method: effect of copper precursors on the properties of CuS, Mater. Chem. Phys. 239 (2020) 122030.
[44] T. Gulin-Sarfraz, G.N. Kalantzopoulos, J.-E. Haugen, L. Axelsson, H. Raanaas Kolstad, J. Sarfraz, Controlled Release of Volatile Antimicrobial Compounds from Mesoporous Silica Nanocarriers for Active Food Packaging Applications, Int. J. Mol. Sci. 23 (13) (2022) 7032.
[45] T. Gulin-Sarfraz, J. Zhang, D. Desai, J. Teuho, J. Sarfraz, H. Jiang, C. Zhang, C. Sahlgren, M. Lindén, H. Gu, Combination of magnetic field and surface functionalization for reaching synergistic effects in cellular labeling by magnetic core–shell nanospheres, Biomater. Sci. 2 (12) (2014) 1750–1760.
[46] H. Fissan, S. Ristig, H. Kaminski, C. Asbach, M. Epple, Comparison of different characterization methods for nanoparticle dispersions before and after aerosolization, Anal. Methods 6 (18) (2014) 7324–7334.
[47] A. Dhawan, V. Sharma, Toxicity assessment of nanomaterials: methods and challenges, Anal. Bioanal. Chem. 398 (2010) 589–605.
[48] Z. Zheng, P. Yu, H. Cao, M. Cheng, T. Zhou, L.E. Lee, J. Ulstrup, J. Zhang, C. Engelbrekt, L. Ma, Starch capped atomically thin CuS nanocrystals for efficient photothermal therapy, Small 17 (47) (2021) 2103461.
[49] Z. Xiao, CuS nanoparticles: clinically favorable materials for photothermal applications? Nanomedicine 9 (3) (2014) 373–375.
[50] L. Wang, X. Ma, K. Cai, X. Li, Morphological effect of copper sulfide nanoparticles on their near infrared laser activated photothermal and photodynamic performance, Mater. Res. Express 6 (10) (2019) 105406.
[51] J. Fang, P. Zhang, H. Chang, X. Wang, Hydrothermal synthesis of nanostructured CuS for broadband efficient optical absorption and high-performance photo-thermal conversion, Sol. Energy Mater. Sol. Cells 185 (2018) 456–463.
[52] Y. Li, W. Lu, Q. Huang, C. Li, W. Chen, Copper sulfide nanoparticles for photothermal ablation of tumor cells, Nanomedicine 5 (8) (2010) 1161–1171.
[53] Y. Qiao, Y. Ping, H. Zhang, B. Zhou, F. Liu, Y. Yu, T. Xie, W. Li, D. Zhong, Y. Zhang, Laser-activatable CuS nanodots to treat multidrug-resistant bacteria and release copper ion to accelerate healing of infected chronic nonhealing wounds, ACS Appl. Mater. Interfaces 11 (4) (2019) 3809–3822.
[54] K. Jiang, D.A. Smith, A. Pinchuk, Size-dependent photothermal conversion efficiencies of plasmonically heated gold nanoparticles, J. Phys. Chem. C. 117 (51) (2013) 27073–27080.
[55] Ir.N.G. Özbilgin, B. Ghosh, H. Yamada, N. Shirahata, Size-dependent photothermal performance of silicon quantum dots, J. Phys. Chem. C. 125 (6) (2021) 3421–3431.
[56] S. Wang, A. Riedinger, H. Li, C. Fu, H. Liu, L. Li, T. Liu, L. Tan, M.J. Barthel, G. Pugliese, Plasmonic copper sulfide nanocrystals exhibiting near-infrared photothermal and photodynamic therapeutic effects, ACS Nano 9 (2) (2015) 1788–1800.
[57] L. Li, L.H. Rashidi, M. Yao, L. Ma, L. Chen, J. Zhang, Y. Zhang, W. Chen, CuS nanoagents for photodynamic and photothermal therapies: Phenomena and possible mechanisms, Photo Photodyn. Ther. 19 (2017) 5–14.